Journal of Applied Physics

Antiferroelectric order and Ta-doped $AgNbO_3$ with higher energy storage density

Cite as: J. Appl. Phys. **125**, 204103 (2019); https://doi.org/10.1063/1.5090444
Submitted: 28 January 2019 . Accepted: 06 May 2019 . Published Online: 30 May 2019

Gen Li, Hai Liu, Lei Zhao, Jing Gao, Shiyou Liang, Jingfeng Li, and Jing Zhu

Journal of Applied Physics ARTICLE scitation.org/journal/jap

Antiferroelectric order and Ta-doped $AgNbO_3$ with higher energy storage density

Cite as: J. Appl. Phys. **125**, 204103 (2019); doi: 10.1063/1.5090444
Submitted: 28 January 2019 · Accepted: 6 May 2019 ·
Published Online: 30 May 2019

Gen Li,[1] Hai Liu,[1] Lei Zhao,[2] Jing Gao,[2] Shiyou Liang,[1] Jingfeng Li,[2] and Jing Zhu[1,a)]

AFFILIATIONS

[1]National Center for Electron Microscopy in Beijing, School of Materials Science and Engineering, The State Key Laboratory of New Ceramics and Fine Processing, Key Laboratory of Advanced Materials (MOE), Tsinghua University, Beijing 100084, People's Republic of China
[2]School of Materials Science and Engineering, The State Key Laboratory of New Ceramics and Fine Processing, Tsinghua University, Beijing 100084, People's Republic of China

[a)]**Author to whom correspondence should be addressed:** jzhu@mail.tsinghua.edu.cn. **Telephone:** +86 010-62794026.

ABSTRACT

Antiferroelectric phenomenological theory can well depict the behavior of the antiferroelectric system, but how to quantitatively define the antiferroelectric order parameter based on the experimental results is still an open question. In this work, the reduced antiferroelectric order parameter is proposed based on the direct atomic-scale observation, which can be regarded as an extension of the traditional antiferroelectric order parameter. In addition, the enhancement of energy storage density of Ta-doped silver niobate is discussed using this reduced antiferroelectric order parameter as a tool. It is found that the deeper reason for the increase of energy storage density can be attributed to the decrease of the permittivity χ_0 of the corresponding paraelectric phase, and novel antiferroelectric materials with high energy storage density may be realized on the base of it.

I. INTRODUCTION

In the 1930s, Lev Landau published his famous theory of phase transition depicting second-order phase transition,[1–3] in which the system thermodynamic free energy was presented as the polynomial function of the system order parameter. After that, in the middle of the 20th century, Devonshire applied and completed Landau theory into the study of ferroelectrics.[4–6] Compared with the original Landau theory, Devonshire's theory could partly depict the behavior of first-order ferroelectric phase transition, which is a great progress.

At the same time, researchers also tried to apply the Landau theory in the antiferroelectric system, and the most known attempt belongs to Kittel. In 1951, Kittel defined two local polarizations P_a and P_b as two antiferroelectric order parameters to qualitatively explain some experimental phenomena,[7]

$$G(P_a, P_b, T) = G_0 + f(P_a^2 + P_b^2) + gP_aP_b + h(P_a^4 + P_b^4), \quad (1)$$

where G_0 is the Gibbs free energy of the paraelectric phase and f, g, and h are positive constants.

However, such an expression is not intuitive enough. Since there are four possible electric states, namely, ferroelectric phase, ferrielectric phase, antiferroelectric phase, and paraelectric phase, researchers hope to use only two order parameters to conveniently depict them: $\eta = 0$, $P = 0$ is the paraelectric phase, $\eta \neq 0$, $P = 0$ means the antiferroelectric phase, $\eta = 0$, $P \neq 0$ represents the ferroelectric phase, and $\eta \neq 0$, $P \neq 0$ stands for the ferrielectric phase.[8] Based on such analysis and symmetry changes in transitions, Tolédano and Guennou wrote the following Gibbs free energy for the antiferroelectric system,[8] where the most important coupling term is η^2P^2:

$$G(\eta, P, T) = G_0(T) + \frac{1}{2}\alpha\eta^2 + \frac{1}{4}\beta\eta^4 + \frac{P^2}{2\chi_0} + \frac{1}{2}\delta\eta^2P^2 - EP, \quad (2)$$

where $G_0(T)$ is the Gibbs free energy of the paraelectric phase, $\alpha = a(T - T_c)$, T_c is the Curie temperature of the antiferroelectric phase, χ_0 is the permittivity of the paraelectric phase, and a, β, and δ are positive constants. Under zero electric field, it can be derived from formula (2) that P must be zero when temperature T is lower than T_c. That is to say, the ferroelectric phase can only be induced

by the external electric field but cannot exist as an independent phase, which is absent in Kittel's model.

Furthermore, this model can effectively explain the double hysteresis P-E loops of antiferroelectric materials. From the above Gibbs function, we can derive a characteristic temperature,

$$T_0 = T_c - \frac{\beta}{2\delta a \chi_0}, \tag{3}$$

which corresponds to one critical electric field

$$E_0 = \frac{1}{\chi_0}\left[\frac{-a(T_0 - T_c)}{\delta}\right]^{1/2} = \frac{1}{\chi_0}\left(\frac{\beta}{2\delta^2\chi_0}\right)^{1/2}. \tag{4}$$

For a given temperature $T < T_0$, it could be calculated that there are two critical electric fields $E_A(T)$ and $E_F(T)$, and both are larger than E_0. When the external electric field lies in the interval (E_A, E_F), both the ferrielectric and ferroelectric phases exist; while the external electric field equals $E_A(T)$ [or $E_F(T)$], the ferroelectric (or ferrielectric) will be unstable and result in a phase transition. This is why antiferroelectric materials behave like double hysteresis P-E loops.

However, such models have not given us a specific formula to quantitatively calculate the antiferroelectric order parameter for any particular antiferroelectric system, especially for the situation where each unit cell contains more than two local electric dipoles. In fact, such a situation is very common in many complex oxide antiferroelectric systems such as $PbZrO_3$ and $NaNbO_3$. Silver niobate is also such a complex oxide antiferroelectric material with the perovskite structure.[9]

After silver niobate was first synthesized in the 1950s,[10] researchers mainly focused on analyzing its structure and phase transitions,[11–19] and first-principles calculation was also used.[20–23] In summary, antiferroelectric phase Pbcm and ferrielectric phase $Pmc2_1$ exist simultaneously in the $AgNbO_3$ system below 340 K, but the $Pmc2_1$ phase occupies less volume fraction.[17,24] However, much attention was not attracted until Fu *et al.* first realized a polarization of up to 52 $\mu C/cm^2$ in the $AgNbO_3$ polycrystal with double-hysteresis P-E loops in 2007,[17] and an upsurge of research on the performance of $AgNbO_3$ appeared. In 2016, Tian *et al.* realized an energy storage property of 2.1 J/cm^3 in $AgNbO_3$.[24] When doped with Mn, W, and Bi, the energy storage density was improved to 2.5 J/cm^3, 3.0 J/cm^3, and 3.3 J/cm^3, respectively.[25–27] In 2017, a large breakthrough was made by Zhao *et al.*, who improved the energy storage density to 4.2 J/cm^3 using Ta as the doping element.[28]

Comparing the P-E loop of pure and Ta-doped $AgNbO_3$,[24,28] the saturated polarization was almost a constant value of 30 $\mu C/cm^2$ before and after Ta doping, while the critical electric field E_A obviously increased: the E_A of $AgNbO_3$ was 52 kV/cm, but abruptly increased to 130 kV/cm when doped with 15% tantalum. People previously interpreted this phenomenon as the enhancement of antiferroelectricity caused by doping elements,[27,28] but it is only an explanation of the macroscopic measurement results and does not elucidate material properties at the microscopic level. In this work, we will first introduce a reduced antiferroelectric order parameter for complex oxide antiferroelectric materials based on the experimental atomic-scale images, and then use it to interpret the enhancement of energy storage density of silver niobate after doping.

II. EXPERIMENTAL

$AgNbO_3$ and $Ag(Nb_{1-x}Ta_x)O_3$ ceramics ($x = 15$ mol. %) were prepared by the conventional solid-state reaction method using Ag_2O (≥99.7%), Nb_2O_5 (≥99.99%), and Ta_2O_5 (≥99.99%) powders as the raw materials. These oxide powders were mixed using a planetary ball mill with anhydrous ethanol at 250 rpm for 24 h, in a nylon jar with zirconia ball media. The dried powder mixture was pressed into disks of 20 mm in diameter and 2 mm in thickness, and calcined at 900 °C for 6 h in an O_2 atmosphere. The calcined powders were milled again and pressed into disks of 8 mm in diameter and 1.2 mm in thickness, followed by cold isostatic pressing under 220 MPa for 1.5 min. After that, samples were sintered at 1100 °C for 6 h in the O_2 atmosphere to prevent the possible decomposition of the silver oxide at a high temperature.

Conventional TEM investigations were performed using a FEI TECNAI $G^2$20 TEM with a double tilting stage, operating at 200 kV. High resolution scanning transmission electron microscope (HRSTEM) experiments were performed using a spherical aberration-corrected Titan Themis transmission electron microscope (TEM) with a double tilting stage, operating at 300 kV, and the STEM detector was a high angle annular dark field (HAADF) detector, with a camera length of 115 mm and the corresponding collection semiangle range is 48–200 mrad. Samples for TEM and STEM experiments were first mechanically polished to 30 μm. After that, a dimpling grinder was used to grind a curved pit on the sample surface. The thickness of the pit bottom is about 10 μm. Then, samples were ion-milled to reach electron transparency with the Gatan PIPS 695 system, in which Ar-ion beams operated at 0.1–4 kV. Using the MacTempas software, the diffraction patterns of the $AgNbO_3$ crystal were simulated. All the image filtering, peak finding, Gaussian fitting, and statistic work were performed with the self-made MATLAB code.

III. RESULTS AND DISCUSSION

High resolution HAADF images of $AgNbO_3$ and Ta-doped $AgNbO_3$ samples under the pseudocubic $[110]_c$ zone axis were obtained, as shown in Figs. 1 and 2. In our experiments, the STEM fast scanning direction was perpendicular to the displacement direction of the B-site atoms, making the drifting effect very small when picking up vertical positions of each horizontal row of atoms;[29] hence, it is reliable to analyze the atomic displacements between different horizontal rows.

Figures 1(a) and 1(b) are simulated and experimental diffraction patterns of $AgNbO_3$ with the Pbcm structure, and Fig. 1(c) is the HAADF image of $AgNbO_3$. Both niobium and tantalum cations possess two opposite displacement $[1\text{–}10]_c$ directions, forming wavy $(1\text{–}10)_c$ atomic planes. One colored crystal unit cell is shown in Fig. 1(c), in which orange spots and green spots stand for silver atoms and niobium atoms, respectively. The illustration in the upper right corner of Fig. 1(c) is its Fourier transform, which is consistent with the experimental pattern of Fig. 1(b) and the simulated pattern of Fig. 1(a), suggesting that the phase structure observed in Fig. 1(c) is Pbcm.

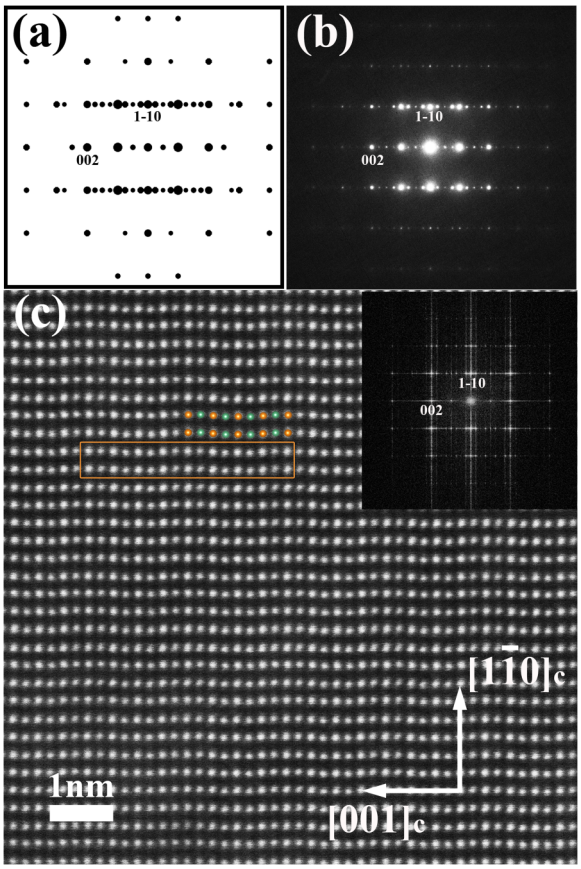

FIG. 1. The diffraction pattern and HAADF image of $AgNbO_3$. (a) Diffraction simulation of silver niobate with the Pbcm structure; (b) experimental diffraction pattern of $AgNbO_3$; (c) STEM-HAADF image of $AgNbO_3$, and its Fourier transform is shown in the upper-right corner.

Figure 2 shows the HAADF image of Ta-doped $AgNbO_3$ and its Fourier transform, which is consistent with that of the Pbcm phase of $AgNbO_3$ shown in Fig. 1(c), suggesting that the phase structure of Ta-doped $AgNbO_3$ observed is also Pbcm. Because the radii and valences of tantalum and niobium cations are almost identical, tantalum cations will take up the positions of niobium cations after doping. Figures 2(b) and 2(c) are magnified views of the yellow rectangular area in Fig. 2(a) and the orange rectangular area in Fig. 1(c), respectively, and it can be seen that the undulation degree of $(1–10)_c$ atomic plane in Fig. 2(b) is a little bit smaller than that in Fig. 2(c). It is worth pointing out that the nuclear charge of tantalum atom is larger than that of niobium, which enhances the scattering of electrons by the B-site atomic columns, and makes the brightness difference between A- and B-site atomic columns decrease in the image.

As discussed Sec. I, Tolédano's antiferroelectric phenomenological model theoretically depicts the behavior of the antiferroelectric system from the view of symmetry, but how to quantitatively define the antiferroelectric order parameter and use it to analyze

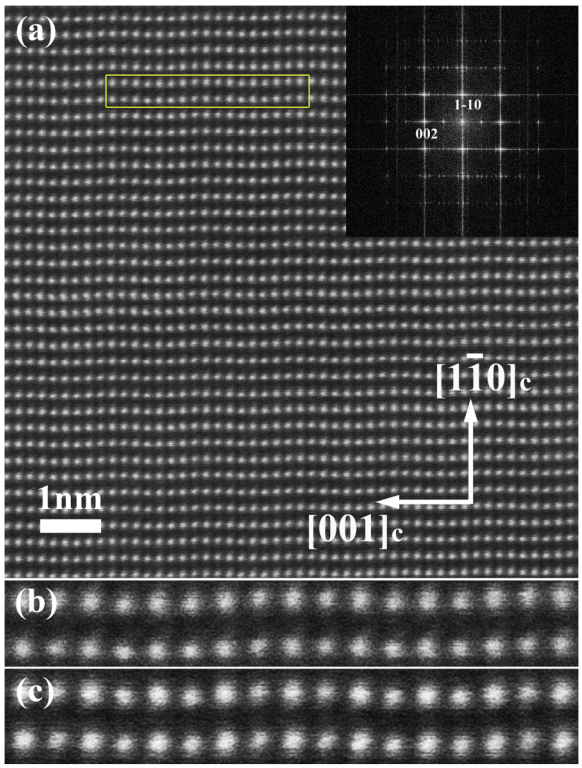

FIG. 2. (a) HAADF image of Ta-doped $AgNbO_3$, and its Fourier transform is shown in the upper-right corner; (b) a magnified view of the yellow rectangular area in (a); (c) a magnified view of the orange rectangular area in (c).

the experimental behavior is still an open question. In the following, a new parameter will be proposed to depict such systems based on the experimental atomic resolution images.

Denoting y_{ij} as the coordinate along the $[1–10]_c$ direction (vertical direction of the image) of the jth atom located in the ith unit cell. Since the displacements of silver and niobium atoms occur in the $[1–10]_c$ direction, for atoms in the ith unit cell, it is reasonable to quantitatively define the so-called reduced antiferroelectric order parameter using the following formula:

$$\eta(i) = \frac{d}{n_i \Delta x_i} \sum_j |y_{ij} - \overline{y_{ij}}| V_{ij}, \tag{5}$$

where n_i is the number of atoms in the ith unit cell, V_{ij} is the chemical valence, which is +1 for silver and +5 for niobium, Δx_i is the distance between closest atoms along the $[001]_c$ direction (horizontal direction of the image) using pixel as a unit, and d is the real distance between closest atoms along the $[001]_c$ direction.

Assuming m as the number of unit cells obtained from images, the reduced order parameter can be calculated as the average value of different $\eta(i)$,

$$\eta = \overline{\eta(i)} = \frac{1}{m} \sum_i \frac{d}{n_i \Delta x_i} \sum_j |y_{ij} - \overline{y_{ij}}| V_{ij}. \tag{6}$$

η is called the reduced order parameter because its value is based on the measurement of cation displacement, which is positively correlated to the value of real localized dipole but not identical.[30] For the simplicity of mathematics, the unit of η is pm because V_{ij} is chemical valence but not charge of cations.

The physical meaning of formula (5) is clear: each localized electric dipole moment is proportional to the product of cation's displacement and valence.[26] The summation of the absolute values of localized dipole moments in a unit cell is the reduced antiferroelectric order parameter η, which is consistent with Tolédano's model:[8] in the paraelectric phase, there is no ion displacement and η is zero; in the ferroelectric phase, all the ions have the same displacement vector, every y_{ij} is equal to $\overline{y_{ij}}$ and η is still zero; but in the antiferroelectric phase and in the ferrielectric phase, different $y_{ij} - \overline{y_{ij}}$ can be positive or negative, hence η must be a positive value.

In our experiments, about 6000 unit cells were found in $AgNbO_3$ images, and more than 10 000 unit cells were found in Ta-doped $AgNbO_3$ images. Frequency distribution histograms (FDH) of $\eta(i)$ in pure $AgNbO_3$ and Ta-doped $AgNbO_3$ are drawn in Fig. 3, and the corresponding reduced antiferroelectric parameter η is calculated as 33.0 pm and 25.7 pm, respectively.

Figure 3 shows frequency distribution histograms and Gaussian fitting results of the reduced antiferroelectric parameter in $AgNbO_3$ and Ta-$AgNbO_3$, and each frequency distribution histogram contains 32 intervals. The red histogram stands for the pure phase $AgNbO_3$, and the blue one stands for the Ta-doped $AgNbO_3$. It is obvious that the averaged reduced antiferroelectric order parameter η decreases after doping, which is consistent with previous research: Levin *et al.* found that the magnitudes of Nb and Ta displacements are reduced in $AgNb_{1/2}Ta_{1/2}O_3$ compared with those in $AgNbO_3$ and $AgTaO_3$.[31] Although in our research the doping concentration 15% is lower than 50% in $AgNb_{1/2}Ta_{1/2}O_3$, they still possess the same tendency to decrease.

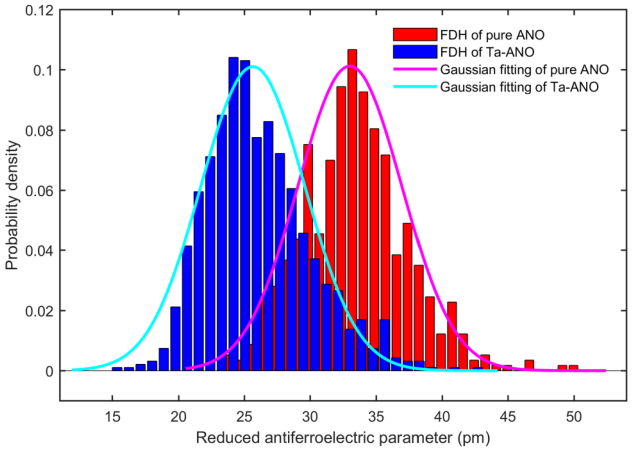

FIG. 3. Frequency distribution histograms and Gaussian fitting results of reduced antiferroelectric order parameters in ANO and Ta-ANO, and each FDH contains 32 intervals.

The stable condition for this system is that the partial derivatives of the free energy function (2) to two order parameters are zero,[8]

$$\begin{cases} \dfrac{\partial G}{\partial \eta} = \eta(\alpha + \beta\eta^2 + \delta P^2) = 0, \\ \dfrac{\partial G}{\partial P} = \dfrac{P}{\chi_0} + \delta\eta^2 P - E = 0. \end{cases} \tag{7}$$

Then, we can calculate the order parameters η and P in the stable state,

$$P(1 + \delta\chi_0\eta^2) = \chi_0 E, \tag{8}$$

$$\eta^2 = -\frac{1}{\beta}(\alpha + \delta P^2). \tag{9}$$

In the antiferroelectric phase, we have

$$\eta_0^2 = -\frac{\alpha}{\beta}, \tag{10}$$

and in the ferrielectric phase $P \approx \frac{E}{\delta\eta^2}$, $\eta \approx \eta_0$.

When external electric field E is relatively small, we have $\delta\chi_0\eta^2 \gg 1$, an approximation of formula (8) is

$$P \approx \frac{E}{\delta\eta^2} \approx -\frac{\beta E}{\alpha\delta}, \quad \frac{dP}{dE} \approx -\frac{\beta}{\alpha\delta}. \tag{11}$$

For antiferroelectric materials, the energy storage density can be roughly written as the product between the saturated polarization P_S of ferroelectric phase, and the critical electric field E_A of antiferroelectric–ferroelectric transition. On the other hand, the influence of Ta-doping is to significantly increase the critical electric field E_A.[22,26]

In Tolédano's model, the double-hysteresis loop of antiferroelectric materials only exists below the critical temperature T_0 given in formula (3). Under different temperature $T < T_0$, the critical electric field E_A and E_F must be larger than the critical value E_0 given in formula (4).

It can be derived from formulas (10) and (11) that

$$\delta \approx \frac{1}{\eta_0^2 \dfrac{dP}{dE}}. \tag{12}$$

Formula (4) can be written as

$$E_0 \approx \frac{dP}{dE}\frac{\eta_0^2\beta^{1/2}}{\chi_0^{3/2}2^{1/2}}. \tag{13}$$

As shown in formula (13), E_0 is proportional to the square of the antiferroelectric order parameter η_0 under zero electric field and proportional to the slope of the P-E loop near the origin, so the increase of the antiferroelectric order parameter can improve the energy storage density; on the other hand, E_0 is inversely proportional to $\chi_0^{3/2}$, where χ_0 is the permittivity of the paraelectric phase; hence, higher permittivity of the paraelectric phase will cause lower energy storage density. After doping Ta element in silver niobate, both the slope of the P-E loop near the origin and the antiferroelectric order parameter η_0 under zero electric field decreased a little, as

shown in the analysis above; but the permittivity χ_0 of paraelectric phase dropped obviously.[32] Therefore, the overall result is the obvious increase of E_0, which further causes the increase of the critical electric field E_A.

Furthermore, we can also extract a strategy to design electrostatic energy storage material with high performance: first, to find one material with large antiferroelectric order parameter η_0 under zero electric field, then to decrease the permittivity of its paraelectric phase as much as possible with different processes such as doping, and to ensure that the antiferroelectric order parameter η_0 does not drop too much. Such a design can significantly improve the critical electric field E_A of antiferroelectric–ferroelectric phase transition and further improve the energy storage density.

IV. CONCLUSION

To conclude, in view of the limitation of the traditional antiferroelectric phenomenological model, we proposed a concept on the reduced antiferroelectric order parameter based on the experimental atomic-scale images for complex oxide antiferroelectric materials. Then, using it as a tool in the framework of the phenomenological model, we found that the enhancement of energy storage density of silver niobate with Ta doping can be attributed to the decrease of permittivity χ_0 of the corresponding paraelectric phase. This work brings about a deeper understanding of antiferroelectric order parameter at the atomic level and gives us a novel strategy to design antiferroelectric materials with high energy storage density.

ACKNOWLEDGMENTS

This work was financially suppported by the Chinese National Natural Science Foundation (NNSFC) (Nos. 51390471, 51527803, and 51761135131), the National 973 Project of China (No. 2015CB654902), and the National Key Research and Development Program (No. 2016YFB0700402). This work made use of the resources of the National Center for Electron Microscopy in Beijing.

REFERENCES

[1]L. Landau, Nature **138**, 840 (1936).
[2]L. Landau, JETP **7**, 19 (1937).
[3]L. Landau, JETP **7**, 627 (1937).
[4]A. F. Devonshire, Philos. Mag. **40**, 1040 (1949).
[5]A. F. Devonshire, Philos. Mag. **42**, 1065 (1951).
[6]A. F. Devonshire, Adv. Phys. **3**, 85 (1954).
[7]C. Kittel, Phys. Rev. **82**, 5 (1951).
[8]P. Tolédano and M. Guennou, Phys. Rev. B **94**, 014107 (2016).
[9]M. Yashima M, S. Matsuyama, R. Sano, M. Itoh, K. Tsuda, and D. S. Fu, Chem. Mater. **23**, 1643 (2011).
[10]M. H. Francombe and B. Lewis, Acta Crystallogr. **11**, 175 (1958).
[11]A. Kania, K. Roleder, and M. Łukaszewski, Ferroelectrics **52**, 265 (1984).
[12]M. Verwerft, G. V. Tendeloo, J. V. Landuyt, W. Coene, and S. Amelinckx, Phys. Status Solidi A **109**, 67 (1988).
[13]M. Verwerft, D. V. Dyck, V. A. M. Brabers, J. V. Landuyt, and S. Amelinckx, Phys. Status Solidi A **112**, 451 (1989).
[14]A. Kania, Ferroelectrics **205**, 19 (1998).
[15]J. Fábry, Z. Zikmund, A. Kania, and V. Petříček, Acta Crystallogr. Sect. C Cryst. Struct. Commun. **56**, 916 (2000).
[16]A. Ratuszna, J. Pawluk, and A. Kania, Phase Transit. **76**, 611 (2003).
[17]D. S. Fu, M. Endo, H. Taniguchi, T. Taniyama, and M. Itoh, Appl. Phys. Lett. **90**, 252907 (2007).
[18]P. Sciau, A. Kania, B. Dkhil, E. Suard, and A. Ratuszna, J. Phys. Condens. Matter **16**, 2795 (2004).
[19]I. Levin, V. Krayzman, J. C. Woicik, J. Karapetrova, T. Proffen, M. G. Tucker, and I. M. Reaney, Phys. Rev. B **79**, 104113 (2009).
[20]I. Grinberg and A. M. Rappe, AIP Conf. Proc. **677**, 130 (2003).
[21]M. K. Niranjan and S. Asthana, Solid State Commun. **152**, 1707 (2012).
[22]H. Moriwake, C. A. J. Fisher, A. Kuwabara, and D. S. Fu, Jpn. J. Appl. Phys. **51**, 09LE02 (2012).
[23]M. Yashima and S. Matsuyama, J. Phys. Chem. C **116**, 24902 (2012).
[24]Y. Tian, L. Jin, H. F. Zhang, Z. Xu, X. Y. Wei, E. D. Politova, S. Y. Stefanovich, N. V. Tarakina, I. Abrahams, and H. X. Yan, J. Mater. Chem. A **4**, 17279 (2016).
[25]L. Zhao, Q. Liu, S. J. Zhang, and J. F. Li, J. Mater. Chem. C **4**, 8380 (2016).
[26]Y. Tian, L. Jin, H. F. Zhang, Z. Xu, X. Y. Wei, G. Viola, I. Abrahams, and H. X. Yan, J. Mater. Chem. A **5**, 17525 (2017).
[27]L. Zhao, J. Gao, Q. Liu, S. J. Zhang, and J. F. Li, ACS Appl. Mater. Interfaces **10**, 819 (2018).
[28]L. Zhao, Q. Liu, J. Gao, S. J. Zhang, and J. F. Li, Adv. Mater. **29**, 1701824 (2017).
[29]C. Ophus, J. Ciston, and C. T. Nelson, Ultramicroscopy **162**, 1 (2016).
[30]A. K. Yadav, C. T. Nelson, S. L. Hsu, Z. Hong, J. D. Clarkson, C. M. Schlepütz, A. R. Damodaran, P. Shafer, E. Arenholz, L. R. Dedon, D. Chen, A. Vishwanath, A. M. Minor, L. Q. Chen, J. F. Scott, L. W. Martin, and R. Ramesh, Nature **530**, 198 (2016).
[31]I. Levin, J. C. Woicik, A. Llobet, M. G. Tucker, V. Krayzman, J. Pokorny, and I. M. Reaney, Chem. Mater. **22**, 4987 (2010).
[32]M. Valant, A. Axelsson, and N. Alford, J. Eur. Ceram. Soc. **27**, 2549 (2007).